

Energetics of pathways enabled by experimentally detected radicals during catalytic, plasma-assisted NH₃ synthesis

Tsung-Wei Liu,^a Fnu Gorky,^b Maria L. Carreon,^b Diego A. Gómez-Gualdrón^{a*}

^a Department of Chemical and Biological Engineering, Colorado School of Mines, Golden CO 80401, USA

^b Department of Chemical Engineering, South Dakota School of Mines, Rapid City SD 57701, USA

ABSTRACT: Plasma-assisted catalysis is emerging as an alternative to several thermocatalytic processes. For ammonia synthesis, it could make the process milder, which would help production decentralization and compatibility with renewable energy. However, one major obstacle preventing optimization of the plasma-assisted process is the incipient mechanistic understanding of ammonia formation on plasma-exposed catalysts. Here, emission spectroscopy detects N• and H• radicals in plasma phases generated from N₂/H₂ mixtures even at atmospheric pressure, which are bound to enable new catalyst-involved pathways not considered in previously reported kinetic models for ammonia synthesis. Thus, we comprehensively examined, via density functional theory (DFT) calculations, the energetics (favorability) of 51 reactions on Fe, Ni, Co, Pd, Ga, Sn, Cu, Au, and Ag. Enthalpic barriers for Eley-Rideal (ER) reactions involving N• and H• radicals were found to be negligible and hence supportive of: *i*) plausible NNH formation and consequent prominent role of the associative pathway to form NH₃ (consistent with some experimental reports detecting surface-bound N_xH_y species), *ii*) likelihood of N• adsorption taking over N₂* dissociation as the primary source of surface bound N*, and *iii*) probable dominance of ER hydrogenation reactions over Langmuir-Hinshelwood (LH) ones. The energetics herein presented will allow thoroughly studying pathway competition in future kinetic models, but numbers calculated here already suggest that the dominant pathway may change with metal identity. For instance, N₂H_y dissociation favorability becomes competitive with ER hydrogenation earlier in the hydrogenation sequence in the more nitrophilic the metals. Yet, the calculated favorability of ER reactions is also already consistent with the weaker dependence of initial NH₃ turnover frequencies (TOFs) on metal identity compared to the thermocatalytic scenario. With practical implications for computational catalyst screening, TOFs experimentally measured herein for an atmospheric dielectric barrier discharge (DBD) reactor linearly correlate with ΔE_{rxn} for the ER hydrogenation reaction $\text{H}\cdot + \text{HNNH}_2^* \rightarrow \text{HNNH}_3^*$. This descriptor may be robust to exact synthesis conditions, as its correlation with TOFs was maintained for earlier TOF data in a sub-atmospheric radio frequency (RF) reactor.

1. INTRODUCTION

Ammonia is already a crucial chemical due to its widespread use in fertilizer production¹ and could gain further importance in the future as a hydrogen carrier² in a so-called “hydrogen economy.”³ The current yearly demand for ammonia is more than 200 million tons,⁴ with ammonia primarily produced from H₂/N₂ mixtures using a thermocatalytic process known as Haber Bosch (HB).⁵ HB requires high temperature to break the N≡N bonds in N₂ and, in turn, high pressure to alleviate temperature-driven reaction equilibrium limitations. The energy-intensive HB requires allocation of ca. 2% of the world’s energy⁶ and is responsible for a similar share of global CO₂ emissions⁶, which creates a need for powering ammonia production with renewable non-fossil energy. However, the harsh conditions of HB make it so the process cannot be easily turned “on and off”⁷, making it incompatible with the intermittent nature of renewable energy. Hence, it is critical to develop methods to synthesize ammonia under mild conditions,^{7–10} which would bring the

additional benefit of decentralizing ammonia production. For example, it could be produced *in situ* in farms using it for fertilizers.

The key to mild ammonia synthesis is to help the catalyst break N≡N at reasonable rates without having to raise the reactor temperature. A potential way to achieve this is by “electrifying” the process using electric fields,¹¹ electrochemistry¹² or plasmas,¹³ where the electricity could come from, for instance, solar or wind energy.^{14,15} In plasma reactors, electrical power is used to generate a plasma phase where electron collisions with N₂ and H₂ can excite and/or dissociate molecular species. Even without a catalyst, the plasma excitation/dissociation products can react with each other to create N_yH_x species that in turn can excite/dissociate from collisions with electrons,¹⁶ ultimately leading to the formation of some NH₃—and some N₂H₂ depending on the reaction conditions (e.g., the type of plasma).^{17–19} Some authors have suggested that without a proper catalyst most of

the product formation in a plasma reactor occurs at the reactor walls instead of the plasma phase.¹⁶ Probably by adsorptive concentration of plasma species on the wall surface. Intriguingly, the introduction of a metal catalyst into the reactor further increases ammonia production,²⁰ indicating that under a plasma environment a proper catalyst likely does more than concentrate reactive species. The reaction mechanism and the exact role of the catalyst, however, remains unclear and under debate, primarily due to the high complexity of plasma reaction networks,²¹ which also makes effects such as plasma-catalyst synergy difficult to unravel, at least to the extent needed to be predictive and enable rational catalyst design.

In early prominent work, Schneider and coworkers²² developed a microkinetic model aiming to explain ammonia synthesis trends in a dielectric barrier discharge (DBD) reactor. Their model consisted of the Langmuir-Hinshelwood (LH) reactions characteristic of HB and assumed that for the N^* production step the main plasma effect was to create vibrationally excited N_2 ($N_2(v)$), whose dissociation barrier was $nh\nu$ lower than for regular N_2 (n = excitation level, h = plank constant, ν = N_2 vibration frequency). However, the existence of plasma radicals was not considered at the time. More recently, Boegaerts and coworkers²³ developed a zero-dimensional reactor model aiming to explain ammonia synthesis in a DBD, including reactions in the plasma phase explicitly. Their model results suggested that N^\bullet and H^\bullet (and other) radicals form in the plasma phase and that, despite low concentration (e.g., lower concentration than $N_2(v)$), they greatly impact ammonia formation rates due to their involvement in Eley-Rideal (ER) reactions on chemisorbed NH_Y^* ($Y = 0-2$) species on metal surfaces. Notably, the occurrence of ER reactions between plasma radicals and chemisorbed species is consistent with isotopic labeling experiments by Gomez-Ramirez and coworkers.²⁴ Yet, one caveat in the model by Bogaerts and coworkers is that their surface was “generic” (as were the parameters for reactions involving surface-bound species), and surface-bound $N_XH_Y^*$ species were not considered. Regarding the latter, using FTIR spectrometry, Chen and coworkers²⁵ reported the detection of N_2H_Y depending on metal identity (Fe or Ni), indicating the importance of understanding the energetics of interaction of these N_XH_Y species in general with different metals (and reactions involving them).

Other reactions that were not considered in previous kinetic models were the dissolution of N^* and H^* to subsurface sites, which were suggested in our previous experiments²⁰ in a radio frequency (RF) plasma reactor to potentially impact ammonia yields. H^* dissolution through a “hydrogen sink” effect, where H^* dissolution slows down ER hydrogen recombination (a reaction reducing H availability), and N^* dissolution as a precursor step to nitride formation (a reaction reducing N availability). For instance, in the abovementioned experiments,²⁰ metals considered to be good hydrogen sinks presented an inverse correlation between ammonia yield and their tendency to form nitrides (Ga > In > Sn > Ni). Analogously, Iwamoto and coworkers²⁶ found an inverse correlation between ammonia formation rates in a DBD reactor and the formation energy of M_3N clusters (Au > Pt > Pd > Ag > Cu > Fe > Ni). Indeed, calculations with ab initio methods have the potential to provide

clarity to experiments as it can examine reaction events in significantly more controlled fashion than experiments. In one such attempt, Mangolini and coworkers²⁷ used ab initio molecular dynamics (AIMD) to interrogate the impingement of an N^\bullet radical on Cu and Pt surfaces fully covered with H^* . In their simulations, N^\bullet seemed to more easily abstract H^* from Cu than from Pt to form NH_3 , which the authors explained based on the stronger binding of N^* in Pt. However, NH_3 formation in their RF plasma experiments was more efficient in Pt than Cu. This apparent discrepancy could be due to incorrect assumptions on H^* coverage and limiting the simulation of N^\bullet impingement to that particular coverage.

The “time limitations” of AIMD underscore the complementary value of reaction models that can account for the multiple reactions that can happen involving plasma and surface-bound species at larger time scales. This would allow understanding how the different reactions proceed on different metal catalysts, and how the catalyst state changes under different plasma conditions (as there are some differences in reaction conditions among reported experiments). However, these models need to be “complete” (e.g., include all relevant reactions) and use accurate enough reaction parameters. With this in mind, here we aimed to use density functional theory (DFT) calculations to obtain the energetic information that would yield reaction parameters for such a “complete” plasma catalysis model. Note, however, that we set the scope for this work on the analysis of the energetics of reactants, product and transition states on different metals, metal-based energetic trends, and the general plausibility of proposed reactions.

To gauge the range of reactions that could be relevant to a complete model, we first aimed to increase our understanding of the plasma phase composition using emission spectroscopy experiments in a DBD reactor. These experiments complement similar experiments we reported earlier in a radio frequency (RF) reactor²⁰ and are consistent with the presence of H^\bullet and N^\bullet radicals in the plasma phases of both DBD and RF reactors despite their differences in operating pressure. Accordingly, our collected emission spectra (along with earlier reports on surface-bound N_2H_Y detection²⁵) motivated us to specifically interrogate *i*) the adsorption energetics of N_XH_Y species ($X = 0-2$, $Y = 0-3$), *ii*) the energetics of LH reactions involving N_XH_Y species, and *iii*) the energetics of ER reactions involving N_XH_Y species and H^\bullet and N^\bullet radicals. The theoretically studied metals have been experimentally tested here by us and/or elsewhere by us or others as catalysts in plasma-assisted ammonia synthesis. The catalysts correspond to the transition metals Fe, Ni, Co, Pd, Cu, Ag, and Au and the post-transition (low-melting-point) metals Ga and Sn. Finally, we accompany the reaction energetic analysis with the exploration of the potential of energetic data to explain and/or predict trends on experimental data, including measured turn over frequencies (TOFs). As an example of the latter, we examined correlations between reaction energies of studied reactions and TOFs for experiments herein performed as well for others reported in the literature.

2. METHODS

2.1. Experiments.

Reactor Setup. The catalytic activity for different metal electrodes was assessed in an in-house DBD reactor (**Fig. 1**).

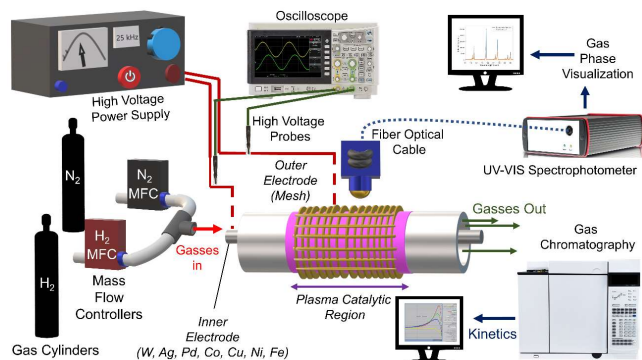


Fig. 1. General schematic and details of the Plasma Catalytic Dielectric Barrier Discharge (DBD) reactor employed

The reaction setup comprises (1) the plasma reactor core, (2) the optical emission spectroscopy system, (3) the oscilloscope, and (4) the gas chromatograph (GC). For the catalytic tests, N_2 and H_2 cylinders were connected to the reactor using mass flow controllers. The reactions were carried out at 25 sccm of total flow rate with equimolar feed ratio of nitrogen to hydrogen (1:1) ($N_2:H_2$) at an average plasma power of 15 Watts. The average bulk temperature of the reactor was 125°C ($\pm 2.8^\circ\text{C}$) with a fan continuously running during reaction time. The applied voltage was measured to be 12 ± 0.5 kV_{pk-pk} with frequency of 25 ± 0.5 kHz. To determine the ammonia synthesis rate, the exhaust gas was sent to the gas chromatograph calibrated for ammonia synthesis. The quantification was performed using an Agilent 7820A GC equipped with a HP-PLOTU column ($30\text{ m} \times 0.320\text{ mm} \times 10\text{ }\mu\text{m}$) and hydrogen as carrier gas. All electrodes were pretreated with hydrogen plasma for 10 minutes at a constant power of 5 watts before conducting the reaction. This had the main purpose of cleaning the metal surface from any native oxide content.

Metal electrodes. All the metal electrodes employed in this study had 2.0 mm diameter and 152 mm length. Alfa-Aesar, 99.995% metal basis wires were employed for Co, Ni, Ag, Cu, and Fe electrodes, wire supplied by Surepure Chemetals Inc. for Pd electrodes, and wire from Midwest Tungsten Service for the W electrode. The high voltage power supply was connected to the reactor using a litz wire and alligator clips. The inner electrodes were placed at the center of the quartz tube with an i.d. of 4 mm and an o.d. of 6.35 mm. The connectors were made of polypropylene to avoid an arc formation. The outer electrode was made of tinned copper mesh acting as the ground electrode.

Electrical Measurements. The electrical characterization was carried out by measuring the applied voltage to the reactor by employing a high voltage probe (Tektronix P6015A). The charge was calculated using the voltage measurement across a capacitor. The two probes are connected to an oscilloscope (Tektronix TDS2014C). The capacitor was connected to the reactor in series with the ground electrode.

Emission Spectroscopy. The light emitted from the discharge was led through an optical system, and the emission spectra of the glow region were measured at the center of the tube. The measurements were recorded using a dual channel UV-vis-NIR spectrophotometer (Avantes Inc., USB2000

Series) in a scope mode. Spectral range from 185 to 1100 nm, using a line grating of 600 lines/mm and a resolution of 0.4 nm. A bifurcated fiber optic cable of 400 μm was employed. The spectral scans were conducted five times for each catalytic cycle with integration time of 3 seconds and scan/average of 100.

2.2. DFT calculations. Plane-wave density functional theory (PW-DFT) calculations were performed using the VASP.5.4.1 ab-initio code.²⁸⁻³⁰ Calculations used the GGA Purdu-Burke-Ernzerhof (PBE) functional³¹ to model the electron exchange and correlation, along with the D2 corrections by Grimme³²⁻³⁴ to explicitly introduce dispersion interactions. An energy cutoff of 400 eV was used to define the basis set of Block waves to construct the solutions to the Kohn-Sham equations. All simulations used spin polarization. Smearing³⁵ at the Fermi level was used to accelerate energy convergence with respect to number of k-points, using the Methfessel-Paxton method of first order with a smearing parameter of 0.03 to keep T^*S under 1×10^{-3} eV. Electronic and atomic configurations were considered converged when energy and forces fell below at least 10^{-5} eV and 10^{-2} eV/ \AA , respectively (10^{-3} eV/ \AA was used for configurations used as input for transition state finding methods).

The bulk unit cells of all metals were optimized, and the slabs for our calculations were cleaved from these unit cells using the Crystal Builder module of Materials Studio.³⁶ Bulk unit cells were optimized using $12 \times 12 \times 12$ Gamma-centered k-point meshes. Lattice constants were within the expected accuracy for PBE ($\sim 2\%$). The cleaved slabs were cut exposing the most stable facet of the metal. The slab for Ga was taken from our previous work.²⁰ The most stable facet for Sn was determined here based on surface energy calculations (see **Table S1**) and were at least 3-layered with at least 1 layer frozen, leaving at least 15 \AA vacuum space between slabs in the direction perpendicular to the surface. A $4 \times 4 \times 1$ k-point mesh was used for slab calculations, as further increasing the mesh density was found to not significantly alter adsorption energies. Calculations on isolated N_xH_y species were done at the gamma-point on a $20\text{ }\text{\AA} \times 20\text{ }\text{\AA}$ orthogonal cell.

Vibrational frequencies were obtained using the finite-displacement method systematically displacing atoms 0.01 \AA in all directions. Generally, vibrations of surface species were decoupled from the vibration of the heavier metal atoms by not performing displacements on them. Transition states were generally found using the climbing-image nudged elastic band (CI-NEB) method³⁷, with the transition state verified to have only one imaginary frequency. Typically, seven images were used to construct the band, which was optimized until forces fell below 5×10^{-2} eV/ \AA . In a few cases, the highest image from the band was found not to have only one imaginary frequency, in which case the transition state was “refined” by using the dimer method³⁸ with the highest band image as input. For the dimer method the electronic and geometric configuration were considered converged when the energy and forces fell below 10^{-8} eV and 10^{-3} eV/ \AA , respectively.

2.3. Sorption and reaction energetics. Adsorption energies (ΔE_{ads}) were calculated as:

$$\Delta E_{ads} = E_{slab+N_xH_y} - E_{slab} - E_{N_xH_y} \quad (1)$$

where $E_{slab+N_xH_y}$ is the energy of the slab with the adsorbed N_xH_y species, E_{slab} is the energy of the slab, and $E_{N_xH_y}$ is the energy of the isolated N_xH_y species. For cases where we estimated the activation energy directly from CI-NEB calculations, the reaction energies were calculated as:

$$\Delta E_{rxn} = E_{slab+} - E_{slab+R} \quad (2)$$

where E_{slab+P} and E_{slab+R} are the energies of the slab with the products and reactants, respectively. Activation energies (E_a) were calculated as:

$$E_a = E_{TS} - E_R \quad (3)$$

where E_{TS} is the energy of the transition state. For cases, where Bronsted-Evans-Polanyi (BEP) relationships were used to estimate activation energies, the needed input reaction energies (ΔE_{rxn}) to get E_a were calculated as:

$$\Delta E_{rxn} = E_{slab+P} + E_{slab} - E_{slab+} - E_{slab+R2} \quad (4)$$

for LH reactions, where E_{slab+P} , $E_{slab+R1}$, and $E_{slab+R2}$ are the energy of the slab with the adsorbed product, reactant 1 and reactant 2, respectively, and as:

$$\Delta E_{rxn} = E_{slab+P} - E_{slab} - E_{R2} \quad (5)$$

for ER reactions, where E_{R2} is the energy of the isolated reactant 2. The BEP relationships used here were derived either by Norskov and coworkers³⁹ or by us from transition state data herein generated. More specifically, for a given reaction directly examined here with transition state finding methods, we found the transition state at least for three metals (chosen as to spread out the values of ΔE_{rxn}), and with the obtained values of E_a and ΔE_{rxn} we derived the corresponding BEP relationships to cost-effectively estimate E_a on the remaining metals. Note that the use of scaling relationships is necessary due to the large number of metal/reaction combinations relevant to plasma-assisted ammonia synthesis.

All the presented energetics was corrected with the zero-point energy (ZPE), which was calculated for every relevant configuration as:

$$ZPE = \sum_{i=1}^n h\nu_i/2 \quad (6)$$

where h is the Plank constant, ν_i is the frequency of vibrational mode i , and n is the number of vibrational modes.

3. RESULTS AND DISCUSSION

3.1. Species detected in the plasma phase. To provide the contrast between metals of highly different nitrophilicity

(see **Section 3.2**), **Fig. 2** presents the plasma emission spectra during catalytic tests for Fe and Ag on a DBD reactor at 15 W power. Emissions at different wavelengths are associated with different plasma species. For example, emission around 656 nm is associated with H_a (atomic hydrogen), which reveals the presence of $H\cdot$ radicals in the plasma phase in our (atmospheric pressure) DBD experiments, with the higher intensity of this emission in Ag versus Fe (**Fig. 2b**) suggesting a higher prevalence of these radicals in the plasma phase when Ag is the catalyst instead of Fe. Notice that we had also detected H_a in our earlier (sub-atmospheric pressure) RF experiments²⁰, suggesting that $H\cdot$ radicals play a role at a wide range of reactor pressures.

Emission around 746 nm corresponds to atomic nitrogen, which would be indicative of the presence of $N\cdot$ radicals. This is a species that we presumed to be formed in our earlier RF experiments²⁰, but that we were not able to quantify due to signal saturation. During the DBD reactor experiments here, however, we do detect differences in emission intensity around 746 nm depending on the metal. For example, the intensity for Ag is higher than for Fe (**Fig. 2c**). One thing to keep in mind is that radicals are expected to be a minority species in the plasma phase, hence their emission signal is several orders of magnitude smaller than, for example, that for N_2 (**Fig. 2a**). Regardless, the emission feature is better defined for H_a , than for N_{atomic} , which led us to collect the emission spectra when only N_2 was fed to the reactor, but with otherwise identical conditions to those for the catalytic tests. At such conditions, the N_{atomic} emission feature becomes more apparent (**Fig. S4**), corroborating that the plasma power used in our DBD catalytic tests is capable of generating $N\cdot$ radicals out of the N_2 gas. In our earlier RF experiments²⁰, it was also possible to compare intensity of metal-free experiments with those including the metal catalyst. For example, the around 10-fold decrease in signal intensity for H_a emissions when the catalyst was introduced was indicative of $H\cdot$ radical adsorption. Given the impossibility of metal-free DBD experiments, here **Table 1** shows the emission intensities associated with different plasma species across different metals (see spectra in **Fig. S6**) relative to the corresponding emission intensity for experiments with a W electrode.

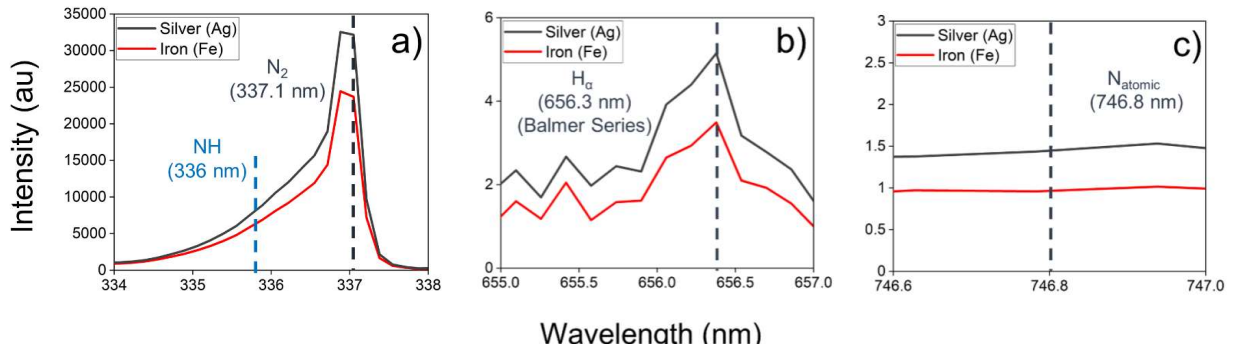


Figure 2. Emission spectra characterization of the plasma phase during ammonia synthesis in the presence of Ag and Fe in a DBD reactor. Emissions at different wavelengths are associated with different species. (a) N_2 and NH wavelength range, (b) H_a (atomic hydrogen) wavelength range, (c) N_{atomic} wavelength range. The reaction temperature was 125 C, $N_2:H_2$ ratio was one, and plasma power was 15 W and. Notice that emissions associated with N_{atomic} are seen more clearly in experiments without co-fed H_2 at 15 W plasma power (**Fig. S4**) or with $N_2:H_2$ ratio of one at 20 W plasma power (**Fig. S5**).

Table 1. Emission intensities for plasma species in metals used in catalytic test in a DBD reactor relative to experiments with the W electrode. Emission wavelengths are 336 nm (NH), 337 nm (N₂), 391 nm (N₂⁺), 656 nm (H_α), 747 nm (N_{atomic}).

Species	Ag	Cu	Pd	Co	Ni	Fe
NH	0.66	0.56	0.61	0.56	0.50	0.43
N ₂	0.64	0.62	0.57	0.52	0.47	0.48
N ₂ ⁺	1.40	1.20	1.11	1.12	1.08	1.16
H _α	5.15	4.71	2.94	4.40	3.72	3.49
N _{atomic}	1.44	1.52	0.89	1.07	1.03	0.92

The differences in relative intensities for the tested metals primarily indicate differences in concentrations of plasma species, which is indicative of the ability of the catalyst to affect the exact composition of the plasma. The most difference in plasma species emission intensities (and thus in species concentrations) tend to occur between Ag and Fe, which again may be due to their markedly different nitrophilicity. The largest intensity difference between any two metals does not exceed 40% for molecular species (N₂ and N₂⁺), increasing to 47% for H_α, 53% for NH, and 70% for N_{atomic}. The relative intensities in **Table 1** present moderate to strong correlations with the adsorption energy for the corresponding radical as calculated from DFT in the **Section 3.2 (Fig. S7)**. H_α intensity correlates with H• adsorption energy (R² = 0.64), which is a significant difference with measurements in our earlier experiments in a RF reactor, for which H_α intensity presents a distinctive volcano-type relationship with this adsorption energy. N_{atomic} intensity correlates with N• adsorption energy (R² = 0.60) and NH intensity with NH• adsorption energy (R² = 0.87). Regardless, we now proceed to discuss DFT calculations motivated with the knowledge that H• and N• radicals are present in the plasma phase.

3.2. Adsorption energies. As we will see through DFT calculations in **Section 3.3**, the presence of H• and N• radicals in the plasma phase is likely the crucial factor facilitating the formation of N_yH_x species. Thus, in this section, we discuss all ZPE-corrected adsorption energies (and adsorption site information) for all N_yH_x species on the most stable (most closely packed) surface for each metal—with the exact values presented in **Table S2**. Due to their lower surface energy, the studied surfaces would be the most abundantly exposed surface on the corresponding metal catalyst. Although we find the ZPE correction for the adsorption energy of a given species to be similar across different metals, without this correction, adsorption strength could be overestimated as much as 0.24 eV (**Table S3**). As previous works suggest an inverse correlation between nitride formation tendency and catalyst performance under plasma conditions, here we discuss the nitrophilicity of nine metals as measured by the N* adsorption energy. Per this metric, nitrophilicity follows the order Ag < Au < Cu < Sn < Ga < Pd < Co < Ni < Fe, making all studied metals less nitrophilic than Fe—the standard catalyst for thermal ammonia synthesis.

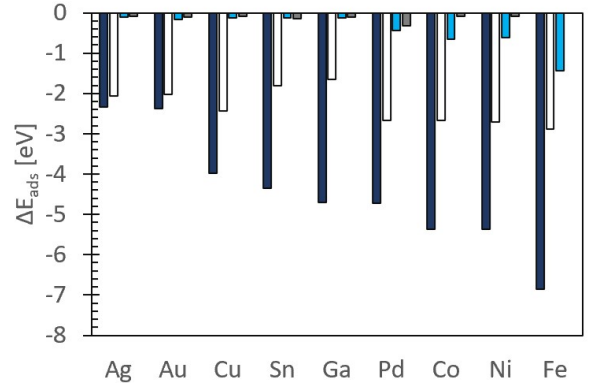


Figure 3. Adsorption energies for N*, H*, N₂*, NH₂* on the studied metal surfaces. N* (dark blue), H* (white), N₂* (light blue), H₂* (gray).

N₂, H₂, N and H adsorption. Adsorption energies for these species are presented in **Fig. 3**, with the corresponding adsorption configuration available on **Fig. S8**. N* is pertinent to the adsorption of N• radicals. N* is most stable on hollow sites on most metals, except on Fe where it is most stable on long-bridge sites. The N* adsorption energy ranges between -2.34 eV in Ag to -6.86 eV in Fe. N₂* is pertinent to the non-dissociative adsorption of N_{2(g)}, which remains as a majority species in the plasma (**Fig. 2a**). However, the adsorption of N₂* is much weaker than N*, ranging between -0.11 eV in Ag and -1.44 eV in Fe. As the nitrophilicity of the metal increases, the adsorption of N_{2(g)} switches from physisorption to chemisorption. The switch point occurs between Ga and Pd, where the adsorption energy jumps from -0.13 eV in Ga to -0.44 eV in Pd, and the adsorption configuration changes from N₂ hovering on Ga (and less nitrophilic metals) to N₂ directly binding a surface site in Pd (and more nitrophilic metals). Intriguingly, this switch occurs despite almost identical N* adsorption energies for Pd and Ga. The N₂ binding occurs vertically on a top site for Pd, Co, Ni, and switches to horizontally on Fe (the most nitrophilic metal).

H* is pertinent to the adsorption of H• radicals, which are presumably more abundant than N• due to the H-H bond being weaker relative to N≡N (0.4 eV vs. 0.9 eV), in consistency with the easier detection of H_α emissions than those of N_{atomic} (**Fig. 2b-c**). H* is most stable on hollow sites on all studied metals, including the less conventional hollow sites of Ga and Sn (**Fig. S2-S3**). The H* adsorption energy ranges between -1.80 eV for Sn and -2.88 eV for Fe. In all metals, the adsorption of H* is weaker than for N*, but stronger than for N₂*. H₂* is pertinent to non-dissociative adsorption of H_{2(g)}, which is the weakest among all species herein studied. H_{2(g)} was physisorbed on all metals except Pd and Fe, adopting a vertically hovering position with adsorption energies in the -0.08 eV to -0.15 eV range. On Pd, H₂* chemisorbs adopting a horizontally bound position on a top site, with an adsorption energy of -0.32 eV. On Fe, we did not find H₂* to be stable, finding it to spontaneously dissociate to 2H* in all our geometry optimization attempts, which is consistent with Fe presenting a negligible barrier for H_{2(g)} dissociative adsorption.

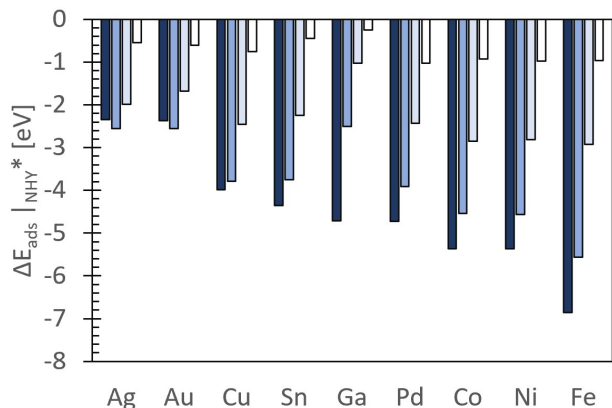


Figure 4. Adsorption energies for NH_Y^* species on the studied metal surfaces. As hydrogenation level increases (as Y changes from 0 to 3) bar color changes from dark blue to white.

N_2^* and H_2^* can also be the basis to discuss adsorption of vibrationally excited N_2 and H_2 , where changes in $h\nu$ as these species adsorb can be inferred from ΔZPE data in **Table S3**. Based on the change of $h\nu$ between the isolated and adsorbed N_2 ($\Delta h\nu_{\text{N}_2}$), N_2^* adsorption energies are directly descriptive of the adsorption of $\text{N}_2(\nu)$ on Ga and less nitrophilic metals. However, for Pd and more nitrophilic metals, $\Delta h\nu_{\text{N}_2}$ ranges between 0.04 eV and 0.12 eV, making the adsorption of $\text{N}_2(\nu)$ in these metals less favorable than for N_2 . The change of $h\nu$ between isolated and adsorbed H_2 ($\Delta h\nu_{\text{H}_2}$) is -0.02 eV on all metals except Pd, making adsorption of $\text{H}_2(\nu)$ slightly more favorable than for H_2 . The opposite is true for $\text{H}_2(\nu)$ on Pd, since $\Delta h\nu_{\text{H}_2}$ is 0.16 eV in this case.

There is a strong correlation between N^* and N_2^* adsorption energies when N_2^* chemisorbs ($R^2 = 0.98$, **Fig. S9a**), but not when N_2 physisorbs ($R^2=0.03$, **Fig. S9b**). This is unsurprising as chemisorption of both N_2^* and N^* is expected to follow the trends from the d-band model⁴⁰ (i.e., higher d-band center equals stronger adsorption), whereas physisorption of N_2^* is not expected to do so. Consistent with this idea, there is no correlation between N^* and H_2^* adsorption energies due to the physisorption character of the latter ($R^2=0.03$, **Fig. S10**). But there is a weak correlation between N^* and H^* adsorption energies ($R^2 = 0.36$, **Fig. S11a**), which becomes strong when Ga and Sn—two post-transition metals that do not follow the d-band model—are obviated ($R^2 = 0.96$, **Fig. S11b**). In other words, Ga and Sn adsorb H^* weaklier than expected from their binding strength to N^* .

NH_Y adsorption. Adsorption energies for these species is presented in **Fig. 4**, with the corresponding adsorption configurations available on **Fig. S12**. NH_Y species form on the catalyst surface under the accepted HB mechanism, but could also form in the plasma and adsorb on the metal surface. For instance, NH was directly detected in our emission spectroscopy experiments. NH^* adsorption energy ranges from -2.55 eV in Au to -5.56 eV in Fe, with NH^* preferably adsorbing on hollow sites on all metals, except on Fe where it preferably adsorbs on long-bridge sites. More hydrogenated NH_Y species tend to adsorb weaklier, with the exception being NH^* in Ag, on which the latter adsorbs weaklier than N^* . NH_2^* adsorption energy ranges from -1.02 eV in Ga and -2.92 eV in Fe, with NH_2^* adsorbing on bridge sites on all metals. NH_3^* adsorption energy ranges between -0.25 eV in Ga to -0.97 eV in Ni, with NH_3 always adsorbing on top

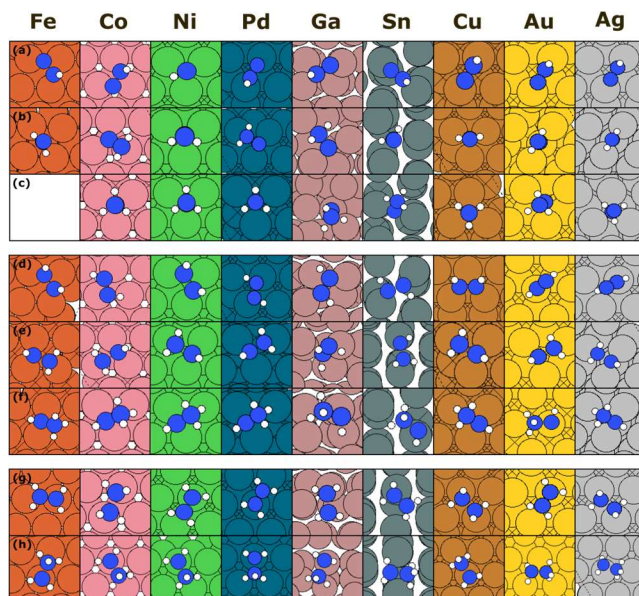


Figure 5. Top-view of most stable adsorption configurations for N_2H_Y species on studied metal surfaces. N-NH_Y species on top row ((a) $Y = 1$, (b) $Y = 2$, (c) $Y = 3$), HN-NH_Y species on middle row ((d) $Y = 1$, (e) $Y = 2$, (f) $Y = 3$), $\text{H}_2\text{N-NH}_Y$ species on bottom row ((g) $Y = 2$, (h) $Y = 3$).

sites. Generally, adsorption weakening with NH_Y hydrogenation is more pronounced as the metal nitrophilicity increases (**Fig. 4**). The correlation between NH_Y^* and N^* adsorption energy weakens as Y increases (from $R^2 = 0.74$ to $R^2 = 0.24$), but it is also stronger when Ga and Sn are ignored (with R^2 ranging from 0.99 to 0.78) (**Fig. S13**). Interestingly, when considering all metals, the adsorption energy of the more hydrogenated species correlates better with H^* adsorption energy. For instance, NH_3^* and H^* adsorption energies correlate with $R^2 = 0.95$ (**Fig. S14**).

N_2H_Y adsorption. An overview of adsorption configurations for these species is shown in **Fig. 5**. N_2H_Y species are seldom considered in the HB mechanism⁴¹, but often considered for electrochemical ammonia synthesis¹² where the associative mechanism is thought to come into play⁴². This mechanism may also be relevant to plasma-assisted ammonia given the experimental detection of N_2H_Y species.²⁵ The associative mechanism starts with the formation of N-NH^* , which preferentially adsorbs horizontally in all studied metals except Ni where it adsorbs vertically on a hollow site. On Au, Ag, Cu, Sn, Ga, and Pd, both N atoms adsorb on hybrid bridge-top positions, whereas on Co, and Fe, both atoms are on bridge positions. N-NH^* adsorption energy ranges from -0.38 in Au to -3.06 eV in Fe. N-NH^* and N^* adsorption energies correlate well for all metals ($R^2=0.80$) but correlate better when Ga and Sn are ignored ($R^2=0.97$) (**Fig. S15**). This is consistent with the tendency by Ga and Sn to adsorb other species weaklier than expected from their binding strength to N^* .

N-NH^* can be hydrogenated through the NH “bead,” which leads to N-NH_2^* and N-NH_3^* formation, with the adsorption energy increasing as hydrogenation increases (**Fig. 6a**), presumably due to the weakening of the N-N bond, which makes the hydrogen-free N increasingly interact more like N^* . In fact, in Fe—the most nitrophilic metal—this is so that N-NH_3 spontaneously breaks into N^* and $\text{NH}_3(\text{g})$. Both N-NH_2^* and N-NH_3^* tend to bind vertically (N-NH_2^*

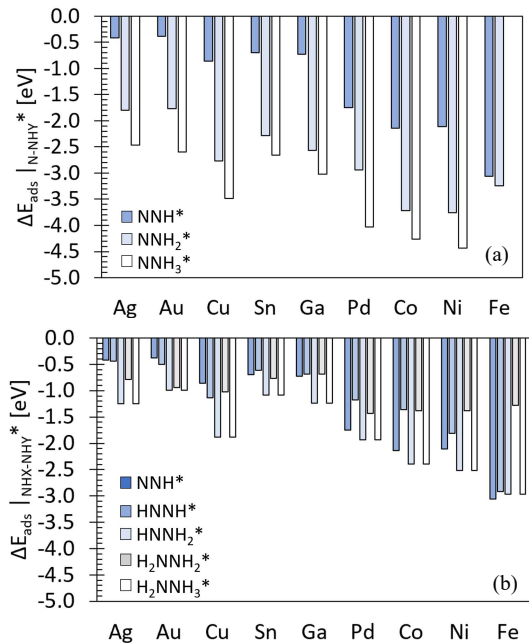


Figure 6. Adsorption energies for species emerging during sequential hydrogenation of NH bead of NNH (a) and during staggered hydrogenation of NNH (b). For each metal, as bar decolorize (from left to right), hydrogenation increases.

tilts on Ga, Pd and Co). In $N-NH_2^*$ the hydrogen-free N tends to bind on bridge sites (binding on hollow sites only on Cu, Sn, Ni), whereas in $N-NH_3^*$ the hydrogen-free-N tends to bind on hollow sites (binding on bridge sites only on Sn) (Fig. 5). Despite the adsorption of $N-NH_V$ becoming more N^* -like as hydrogenation increases, the adsorption energies of $N-NH_2^*$ and $N-NH_3^*$ correlate less with that of N^* ($R^2 \sim 0.7$) than N_2H^* does (Fig. S15). Interestingly, when Ga and Sn metals were ignored, the adsorption energy of $N-NH_3$ correlates better with N^* adsorption energy ($R^2 \sim 0.99$) because the N-N bond between the hydrogen-free N and NH_3 is weak, and the hydrogen-free N is very similar with the simple N^* .

$N-NH^*$ can also be hydrogenated in staggered fashion to form $HN-NH^*$, $HN-NH_2^*$, $H_2N-NH_2^*$ and $H_2N-NH_3^*$. Among these, $HN-NH^*$ and $H_2N-NH_2^*$ are molecular species (diazene and hydrazine, respectively) that tend to adsorb weaker than $HN-NH_2^*$ and $H_2N-NH_3^*$. Therefore, adsorption trends with hydrogenation and metal nitrophilicity, while rationalizable, are not simple (Fig. 6b). $HN-NH^*$ shifts from likely to desorb in Ag ($\Delta E_{ads} = -0.44$) to unlikely to desorb in Fe ($\Delta E_{ads} = -3.12$ eV). Except on Cu, Ni, and Fe, $HN-NH^*$ was most stable on its *trans* configuration. $H_2N-NH_2^*$ adsorption energies range from -0.68 eV on Ga to -1.43 eV on Pd. Similar to NH_3^* , $H_2N-NH_2^*$ adsorption energies correlate better with that of H^* ($R^2 = 0.88$, Fig. S17) than with that of N^* ($R^2 = 0.35$, Fig. S16).

3.2. H and N dissolution. “Adsorption” energies at the most favorable dissolution subsurface sites are presented in Table S2, along with indication of the type of site. Typical dissolution reaction pathways and all transition states are presented in Fig. S18. Again, these calculations were motivated by the hydrogen-sink effect postulated to aid catalyst performance by removing H^* from the surface, hence hindering recombination to $H_2(g)$ and boosting H^* availability for reaction pathways that lead to NH_3 .²⁰ We denoted subsurface

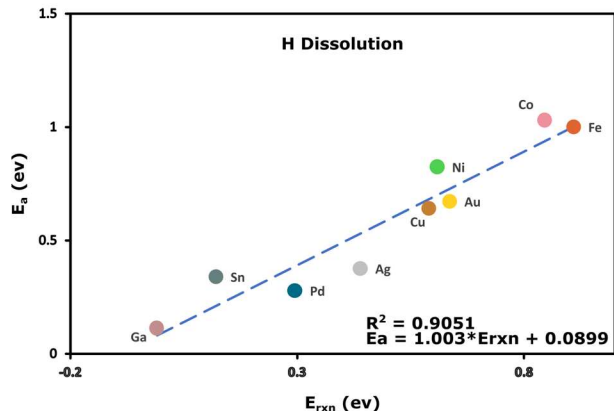
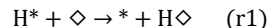


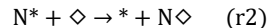
Figure 7. BEP relationship between activation and reaction energies for H dissolution reaction (*r1*). $R^2 = 0.90$.

sites as “ \diamond ” and dissolved H as $H\diamond$, which was generally found to be more stable on octahedral subsurface sites, except on Pd (tetrahedral site), Ga (distorted tetrahedral site) and Sn (distorted hexagonal prism). Pd, as expected from its use in hydrogen membranes⁴³, binds $H\diamond$ more strongly (-2.38 eV) than other metals studied here, with a binding almost as strong as the corresponding H^* adsorption. Metals such as Cu, Co, Ni and Fe also bind $H\diamond$ strongly (between -1.84 eV and -2.10 eV) but noticeable less so than the corresponding H^* . Accordingly, we generally observed positive reaction energies for:



which range from -0.01 eV for Ga to 0.91 eV for Fe, and which present only moderate (inverse) correlation with H^* adsorption energies ($R^2 = 0.54$, Fig S19). However, a strong correlation was found between the reaction and activation energies for the dissolution reaction *r1* ($R^2 = 0.90$, Fig. 7), even though the activation energy for Fe dissolution was taken from ref. ^{44,45}. Metals seem to cluster into three groups based on to what extent hydrogen dissolution is facilitated in them: Ga, Sn, Pd and Ag ($E_a < 0.4$ eV), Cu, Ni, Au (0.6 eV $< E_a < 0.9$ eV) Co and Fe ($E_a > 1.0$ eV).

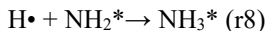
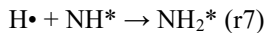
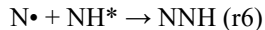
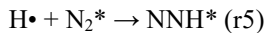
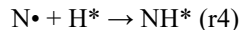
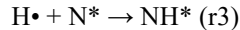
Nitride formation is another process that has been suggested to impact ammonia formation.²⁰ Nitride formation likely requires nitrogen dissolution to the bulk, motivating us to inspect the dissolution reaction *r2*:



The reaction energy for *r2* ranges from -0.15 eV in Ga to 1.61 in Fe, with only a moderate (inverse) correlation with N^* adsorption energies ($R^2 = 0.53$, Fig S20). Similar to *r1*, the inverse correlation arises because the stronger the surface adsorption is, the less likely the subsurface binding is to match it. Given, the strong correlation between reaction and activation energies ($R^2 = 0.96$, Fig. S21), the less nitrophilic metals tend to have lower dissolution barriers. The exception is Ga and Sn, whose low activation energy for *r2* (and *r1*) is likely due to their “open” structures which allows for metal atom mobility as N (and also H) goes from the surface to the subsurface. For instance, an inspection to Fig. S18 show the significant rearrangement of metal atoms in the dissolution transition states in Sn.

3.3. ER reactions. Given the experimentally detected presence of radicals in N_2/H_2 plasmas, one of the major differences between plasma-assisted and thermocatalytic ammonia synthesis is that in the former ER reactions where plasma radicals react with surface-bound species become plausible.

ER activation barriers. In our previous work²⁰, we assumed a scaling relationship proposed by Bird et al.⁴⁶ to estimate barriers for ER reactions involving molecular species to hold for ER reactions involving radicals. On the other hand, Boggaerts and coworkers have recently assumed energy barriers for ER reactions involving radicals to be zero.⁴⁷ Thus, to examine the typical barrier for ER reactions, we chose to directly study the reaction coordinates for reactions $r3$ to $r8$ using CI-NEB calculations on at least three metals each:



The above reactions represent a diversity of ER reaction scenarios. For instance, whereas for $r3$ we expected $H\bullet$ to be able to land directly on N to form NH^* without a barrier, for $r4$ we were uncertain whether NH having to flip upon $N\bullet$ landing on H^* would manifest on a barrier. $r5$ represents a scenario where a radical collides with a weakly bound molecule, $r6$ where a radical has to “scoop up” a strongly bound species, $r7$ and $r8$ where upon collision with the radical the bound species has to migrate to a different adsorption site. To set up the reactant state for each of these calculations we *i*) took the optimal configuration for the product from **Section 3.2** and displaced either the H or N atom assumed to come from the radical vertically up to 3.0 Å from their position in the product and froze it at that location, *ii*) took the “leftover” surface-bound species (the reactant) and (as needed) moved to the nearest adsorption site known to be optimal for it from **Section 3.2**, *iii*) optimized the reactant state. Once this was done, we built intermediate configurations between reactant and product states using interpolation and ran CI-NEB calculations as described in **Section 2.2**.

A bird’s eye view of energy vs. reaction coordinate plots is presented in **Fig. S22**. Our calculations were unable to reveal a barrier/transition state for any of the tested ER reactions on any of the tested metals. Representative reaction coordinates for $r3$ - $r8$ reactions on assorted metals are presented on **Fig. 8** to gain insights on how these reactions proceed. For $r3$, we observe the reaction to proceed as expected with an $H\bullet$ radical able to simply land on N^* to form NH^* . For $r4$, we observe that a close enough $N\bullet$ radical can abstract surface-bound H^* to form an $NH\bullet$ radical slightly away from the surface, which then rotates as it falls back on the surface as NH^* . For $r5$, we observe that a $H\bullet$ radical on collision course with the surface can attract a “hovering” N_2^* to form $NNH\bullet$ slightly away from the surface, which then lands as NNH^* . For $r6$, we observe that a $N\bullet$ radical close enough to a surface-bound NH^* can abstract the H atom to form a $NH\bullet$ radical that rotates as it lands on the leftover N^* to form NNH^* . For $r7$ (and $r8$), we observe that a $H\bullet$ radical on collision course with the surface can attract a nearby NH^*

(NH_2^*), which starts to move from a hollow (bridge) site to a bridge (top) site to form NH_2^* (NH_3^*).

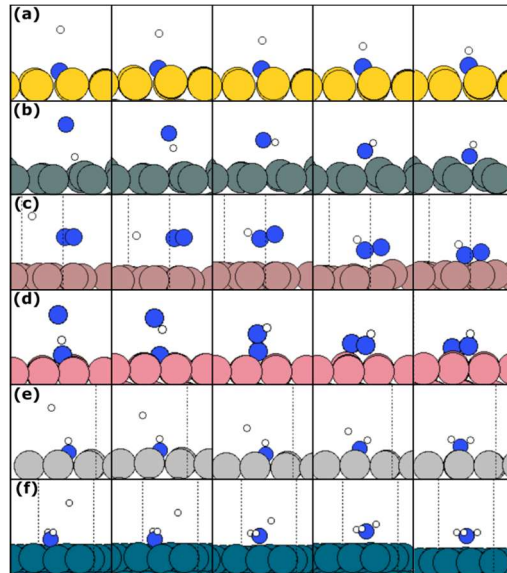


Figure 8. Reaction coordinates for ER reactions $r3$ to $r8$. (a) $r3$ on Au, (b) $r4$ on Sn (c) $r5$ on Ga, (d) $r6$ on Co, (e) $r7$ on Ag, (f) $r8$ on Pd.

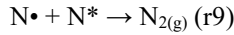
Table 2. Estimated entropic barrier (TS_a) in eV at different temperatures and partial pressures for ER reactions involving the $H\bullet$ or $N\bullet$ radical. The assumption is that the radical loses one degree of freedom in a reactant-like transition state.

P [bar]	H• radical		N• radical	
	T = 398 K	T = 673 K	T = 398 K	T = 673 K
1×10^{-6}	0.32	0.56	0.36	0.64
1×10^{-5}	0.29	0.51	0.33	0.59
1×10^{-4}	0.26	0.47	0.31	0.55
1×10^{-3}	0.24	0.43	0.28	0.50
1×10^{-2}	0.21	0.38	0.26	0.46
1×10^{-1}	0.18	0.34	0.23	0.41
1	0.16	0.29	0.20	0.37

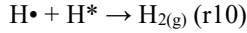
The above suggests that the assumption that ER reactions involving plasma radicals generally do not present energy (enthalpic) barriers is acceptable. Note, however, that ER reactions still must overcome entropic barriers as the inability of our CI-NEB calculations to reveal barriers does not preclude relevant transition states from existing. Rather, the implication is that the transition state elusiveness is due to excessive resemblance to the reactant state (as opposed to product state given the high exothermicity of the reaction). Therefore, the major change between the reactant and transition state for an ER reaction is likely the loss of one translational degree of freedom by the $H\bullet$ or $N\bullet$ radical, with the entropy of activation S_a corresponding to the loss of one third of the entropy the radical possesses in the gas phase. As a reference, then, **Table 2** presents TS_a at 673 K and 398 K. These reaction temperatures correspond to our earlier RF experiments and our current DBD experiments, respectively. Per this calculation, ER reactions involving a $H\bullet$ radical present entropic barriers lower than 0.56 eV and 0.32 eV at 673 K and 398 K, respectively, assuming $H\bullet$ radical concentration is not lower than 10^{-6} bar. Under a similar assumption for concentration, for ER reactions involving a $N\bullet$ radical,

the entropic barriers are lower than 0.64 eV and 0.36 eV at 673 K and 398 K, respectively. Based on these entropic barriers, the fact that $G_a \sim -TS_a$ and the reasonable assumption that for surface reactions $E_a \sim G_a$ (Fig. S25), we will be using a 0.5 eV as a rough threshold when discussing favorability of ER reactions versus surface reactions.

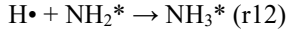
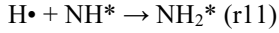
ER reaction energies. Given the negligible energy (or enthalpic) barrier for ER reactions, and the independence of the (low) entropic barrier from metal identity, we focus now on the favorability of ER reaction based on reaction energies. Reaction energies for 20 ER reactions considered in this work are presented in Table S4. These reactions include *i*) recombination reactions where a N^\bullet (H^\bullet) radical collides with N^* (H^*) to make $N_{2(g)}$ ($H_{2(g)}$), *ii*) NH_Y -making reactions, which only lead to ammonia, *iii*) and H_XNNH_Y -making reactions, which lead to diazene, hydrazine, and ammonia. Nitrogen and hydrogen ER recombination are more favorable when the adsorption strength of N^* and H^* , respectively, is weaker. For instance, since Ag adsorbs N^* weaker than on Fe, nitrogen recombination is more favorable on Ag (Fig. S23). Across all metals, nitrogen recombination ($r9$, ΔE_{rxn} ranging from -7.89 eV in Ag to -3.37 eV in Fe):



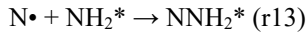
is significantly more favorable than hydrogen recombination ($r10$, ΔE_{rxn} ranging from -2.45 eV in Sn to -1.37 eV in Fe):



Competing with $r9$ and $r10$ are $r3$ and $r4$, which lead to NH^* . Once NH^* is formed, ER hydrogenation can only follow the sequence:



However, $r11$ must compete with $r6$ (which forms NNH^*) and $r12$ must compete with $r13$ (which forms NNH_2^*):



$r6$ and $r13$, however, are more thermodynamically favored (i.e., more exothermic) than $r11$ and $r12$, consistent with a trend where ER reactions involving N^\bullet radicals tend to be more favorable than those involving H^\bullet radicals (Fig. S24). Once NNH^* or NNH_2^* is formed, ER hydrogenation can follow different sequences “assembled” from the following reactions:

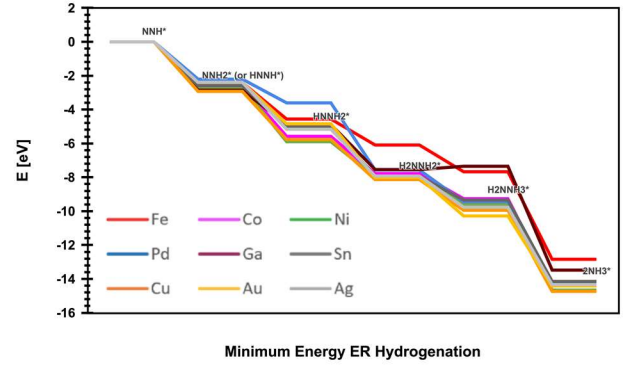
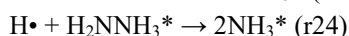
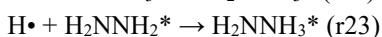
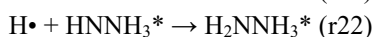
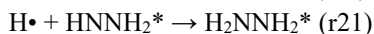
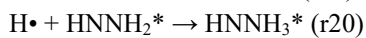
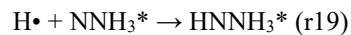
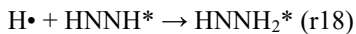
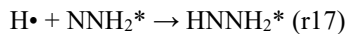
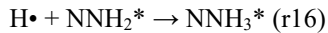
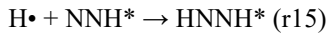
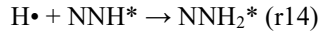
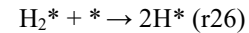
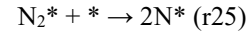


Figure 9. Minimum energy ER hydrogenation pathway for NNH^* on studied metals. For the N_2H_2 intermediate, NNH_2^* is most stable on Ni, Co, Pd, Ga, and Cu, whereas $HNNH^*$ is most stable on Fe, Sn, Au, and Ag.

If we assume that the most thermodynamically favored hydrogenation sequence is dominant, upon formation of NNH^* via $r6$, Fe, Sn, Au, and Ag would follow the hydrogenation sequence $r15$ ($HNNH^*$) \rightarrow $r18$ ($HNNH_2^*$) \rightarrow $r21$ ($H_2NNH_2^*$) \rightarrow $r23$ ($H_2NNH_3^*$) \rightarrow $r24$ ($2NH_3^*$), whereas Ni, Co, Pd, Ga, and Cu would follow the sequence $r14$ (NNH_2^*) \rightarrow $r17$ ($HNNH_2^*$) \rightarrow $r21$ ($H_2NNH_2^*$) \rightarrow $r23$ ($H_2NNH_3^*$) \rightarrow $r24$ ($2NH_3^*$). On the other hand, upon formation of NNH_2^* via $r13$, all metals would follow the hydrogenation sequence $r17$ ($HNNH_2^*$) \rightarrow $r21$ ($H_2NNH_2^*$) \rightarrow $r23$ ($H_2NNH_3^*$) \rightarrow $r24$ ($2NH_3^*$). Notably, hydrazine (a species detected in some plasma-assisted ammonia synthesis experiments^{19,48}) is an intermediate in all the above pathways.

Fig. 9. Illustrates the energetics of these minimum energy hydrogenation sequences for each metal starting from NNH^* . The hydrogenation process is a continuously downhill process except on Ga, where H_2NNH_3 formation is an endothermic step. In the first hydrogenation step, NNH_2 is most stable in most studied metals, except on Fe, Sn, Au, and Ag where $HNNH$ has lower energy. An important observation from Fig. 9 is that the hydrogenation steps tend to become more favorable the less nitrophilic the metal is. However, as H_XNNH_Y hydrogenation increases, dissociation reactions become more likely (see below), in which case hydrogenation would continue individually on the produced NH_X and NH_Y fragments.

3.4. Dissociation reactions. Reaction and activation energies for 10 dissociation reactions are presented in Table S6. We start our discussion with reactions $r25$ and $r26$, which in traditional HB ammonia synthesis are the sole source of N^* and H^* for subsequent NH_Y^* formation:



Using scaling relationships²², we estimate the barrier for $r25$ to range from 1.64 eV on Fe to 6.77 eV on Ag. Again, assuming that entropic contributions for surface reactions are such that E_a and G_a (free energy of activation) are similar (a reasonable assumption for discussion purposes as shown in Fig. S25), then it is likely that above some critical radical concentration, N^\bullet radicals (even as a minority species) are the dominant source of N^* even on Fe. Similarly, using scaling relationships³⁹, we estimate the energy barrier for $r26$ to range from 0.85 eV to 1.27 eV on Ag, Au, Ga, and Sn. Thus,

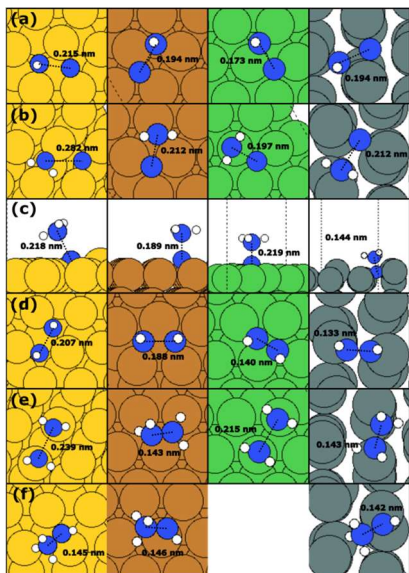
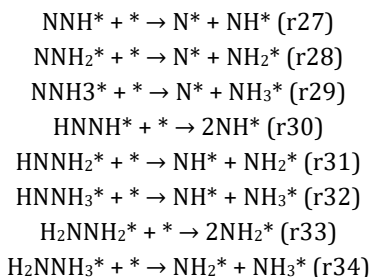


Figure 10. Transition states for dissociation reactions $r27$ (a), $r28$ (b), $r29$ (c), $r30$ (d), $r33$ (e) and $r32$ (f) on Au (yellow), Cu (orange), Ni (green) and tin (gray).

above a critical radical concentration, H^\bullet radicals are the likely dominant source of H^* on these metals. On the other hand, the energy barrier for $r26$ ranges from 0.08 eV to 0.36 eV on Co, Ni, Pd and Cu, which could make $r26$ competitive as a source of H^* (especially on Fe, Ni, Co). Incidentally, the barrier for $r26$ on Fe is likely negligible in consistency with our observation of spontaneous dissociation when attempting to optimize H_2^* .

Regardless of the dominant source for N^* and H^* , in the plasma-assisted process, the reaction energetics discussed so far is supportive of the presence of radicals facilitating the formation of H_xNNH_y species, which could dissociate according to:



Transition states found for these reactions are presented in **Fig. 10**. From H_xNNH_y dissociation energy barriers obtained explicitly here, we derived scaling relationships to infer energy barriers from reaction energies for the same reaction on different metals (**Fig. S26**).

We found the first hydrogenation of N_2^* to NNH^* to already significantly facilitate N-N bond breaking. For instance, while the N_2^* dissociation barrier for Ni was estimated to be 2.57 eV, the NNH^* dissociation barrier on this metal was found to be 0.45 eV. Thus, the barrier for $r27$ was estimated to range between 0.00 eV in Fe to 3.00 eV in Ag. This trend for $r27$ is consistent with general trends for $r28$ - $r34$, whose barriers tended to be lower the more nitrophilic

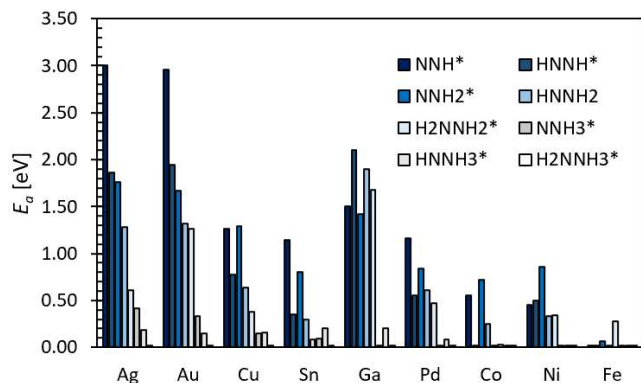


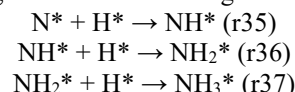
Figure 11. Energy barriers for the dissociation of H_xNNH_y species on studied metal surfaces. For each metal, Y increases from left to right (and for same Y , larger X is placed to the right). Note that 0.00 eV bars were given a 0.02 eV height to facilitate visualization.

the metal was (**Fig. 11**). For instance, on Fe, all H_xNNH_y species dissociate with barriers below 0.5 eV, whereas on Ag, only until hydrogenation creates NNH_3 , does the barrier to break the N-N bond goes below 0.5 eV. Accordingly, on a highly nitrophilic metal such as Fe one can expect dissociation to occur as early as NNH^* is formed, with hydrogenation continuing on N^* and NH^* . On the other hand, following the sequence on **Fig. 9**, on a metal such as Ag, hydrogenation could continue until H_2NNH_3 is formed, at which point dissociation can occur, releasing an NH_3^* and the NH_2 being hydrogenated in a subsequent step.

As inferred from the statements above, an observed general trend is that, as hydrogenation increases, N-N bond breaking tends to become easier. Although the hydrogenation of a given N atom is more influential than the overall hydrogenation of the H_xNNH_y species. For instance, the barrier for NNH_3^* dissociation is lower than for $HNNH_2^*$ dissociation. This trend is more apparent on the less nitrophilic metals. Ga, a moderately nitrophilic metal, is intriguing in that dissociation barriers of H_xNNH_y species tend to remain above 1.0 eV as long as Y stays below 3. Once Y equals 3, the dissociation barrier drops dramatically, at least below 0.2 eV. In this aspect, it is quite different than the slightly less nitrophilic Sn, on which the dissociation of H_xNNH_y species seems to be dramatically easier.

3.5. LH reactions.

Hydrogenation. Under the accepted mechanism for the HB process, hydrogenation occurs through the LH reactions:



Calculated reaction energies for these reactions are shown in **Fig. 12**, along with hydrogenation barriers estimated from scaling relationships using our calculated reaction energies as input. Reactions $r35$ - $r37$ tend toward exothermicity and lower barrier as metal nitrophilicity decreases. Indeed, the barriers for $r35$ - $r37$ tend to be below 1.00 eV for Sn, Cu, Au and Ag, and above 1.00 eV for Fe, Ni, Co, and Pd (with Ga straddling both groups). Thus, only for the former group LH hydrogenation is likely to be competitive with ER one.

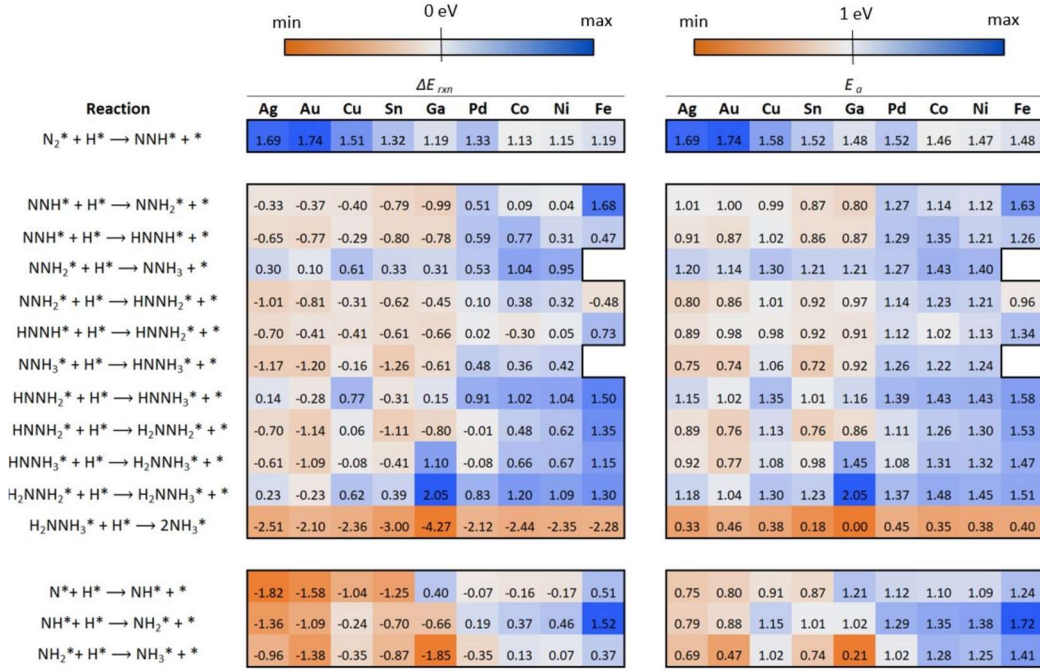
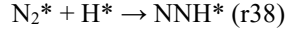


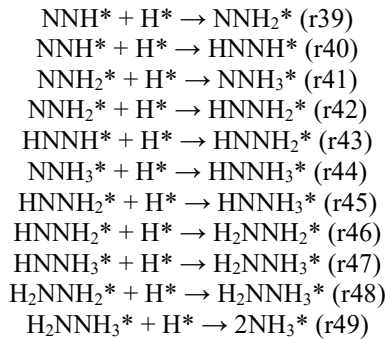
Figure 12. Reaction (ΔE_{rxn}) and activation (E_a) energies for LH hydrogenation reactions. Color scale for ΔE_{rxn} and E_a indicated by the top color bars. Orange and blue indicate more favorable and less favorable reactions, respectively.

As noted from our discussion on ER reactions, formation of NNH can initiate the associative mechanism. An alternative to the ER pathway would be NNH formation through the LH hydrogenation reaction:



However, using a universal scaling relationship³⁹, we estimate barriers of 1.46 eV or higher for $r38$ (Fig. 12). Thus, based on the entropic barriers (Table 2) for the NNH-forming ER reactions $r5$ and $r6$, it is likely that NNH formation is dominated by ER pathways.

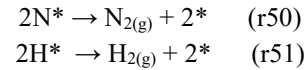
Once NNH is formed, then hydrogenation could occur through the LH reactions:



Similar to $r35$ - $r37$, Fig. 12 shows that $r39$ - $r48$ tend more toward exothermicity and barriers below 1.00 eV on Sn, Cu, Au and Ag and toward endothermicity and barriers above 1.00 eV on Fe, Ni, Co, and Pd (with Ga straddling both groups). The reaction with a commonly low barrier is $r49$, which occurs with a barrier lower than 0.50 eV on all metals. As for the least resistant LH hydrogenation path, for both the least nitrophilic metals in the former group, Ag and Au, with the most nitrophilic metal in the latter group, Fe, the least resistant path to arrive to $H_2NNH_3^*$ is via $r40 \rightarrow r43 \rightarrow r46$

$\rightarrow r48$. For Ag and Au the highest barrier to be overcome is 1.18 eV, 1.04 eV, and 1.30 eV, whereas for Fe is 1.53 eV. For the remaining metals, the least resistance hydrogenation sequence is $r39 \rightarrow r42 \rightarrow r46 \rightarrow r48$, where the lowest barrier to be overcome is 0.8 eV. Comparing the barriers between LH and ER hydrogenation, it is likely that when radical concentration is above some critical value ER hydrogenation dominates, at least until H_2NNH_3 is formed. Once the latter species is formed, the low barrier for $r49$ may make NH_3^* formation via a last LH step competitive with a last ER step.

Recombination. Alternatives to recombination ER reactions $r9$ and $r10$ are LH reactions $r11$ and $r12$:



but in contrast to the ER route, these reactions do present an energy barrier and tend to be more favorable for hydrogen (E_a ranging from 0.48 eV on Sn to 1.18 eV on Pd) than for nitrogen recombination (E_a ranging from 1.10 eV on Ag to 3.29 eV on Fe) (Table S8). Similar to ER recombination, LH recombination of nitrogen and hydrogen correlates inversely with the adsorption strength of N^* and H^* , respectively. The barriers for LH recombination of nitrogen suggest it as unlikely to be competitive with ER nitrogen recombination in any metal. On the other hand, LH recombination of hydrogen could be competitive with the analogous ER reaction on Ga, Sn, Ag, and Au.

3.6. Adsorption and desorption reactions. The (negative of) adsorption energies discussed in Section 3.2. can be considered as the reaction energies for (desorption) adsorption reactions of species that can be found in the plasma phase as molecules or radicals. For instance, adsorption energies for N^* and NH^* can be considered reaction energies for the adsorption of N^\bullet and NH^\bullet radicals, respectively, whereas the negative of the adsorption energies for NH_3^* , $N_2H_2^*$ and $N_2H_4^*$ can be considered reaction energies for the desorption

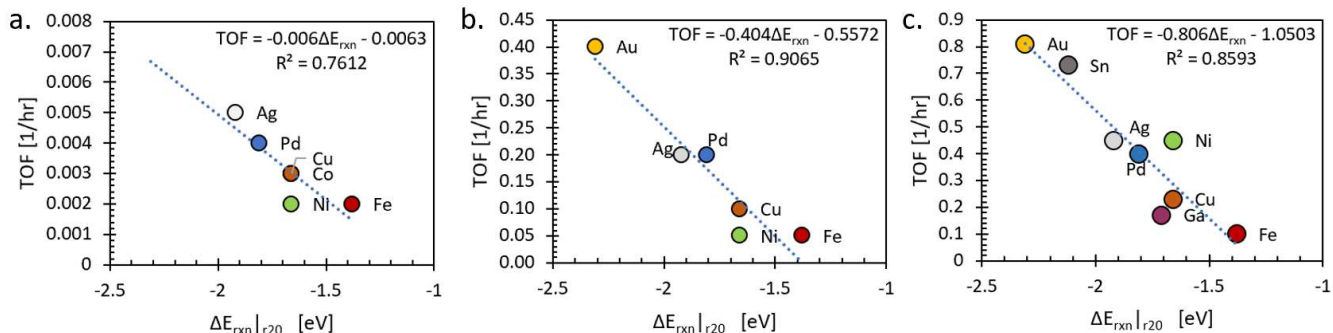


Figure 13. Correlation between turnover frequency (TOF) in various experiments and reaction energy for r_{20} ($\text{H}\cdot + \text{HNNH}_2^* \rightarrow \text{HNNH}_3^*$). a) Current experiments: DBD reactor, $T = 125$ C, $P = 1$ atm, $\text{N}_2:\text{H}_2$ ratio = 1, flow rate = 25 sccm, plasma power = 15 W, b) DBD reactor, T = not reported (no heat exchange), $P = 1$ atm, $\text{N}_2:\text{H}_2$ ratio = 1, flow rate = 100 sccm, applied voltage = 5 kV, taken from ref.²⁶, c) RF reactor, $T = 400$ C, $P = 3.5 \times 10^{-4}$ atm, $\text{N}_2:\text{H}_2$ ratio = 0.25, flow rate = 20 sccm, plasma power = 300 W, taken from ref.²⁰.

of $\text{NH}_{3(g)}$, $\text{N}_2\text{H}_{2(g)}$ and $\text{N}_2\text{H}_{4(g)}$, respectively. The adsorption of radicals is highly exothermic, meaning their desorption is highly endothermic. On the other hand, to what extent molecular species are likely to desorb before they continue to react may depend on the metal. For example, HNNH (diazene) on Fe is less likely to desorb ($\Delta E_{\text{des}} = 3.12$ eV) before it dissociates ($E_a = 0.00$ eV), whereas on Sn, Au or Ag ($\Delta E_{\text{des}} < 0.65$ eV) this desorption may be more competitive with, say, ER hydrogenation to HNNH₂. H_2NNH_2 (hydrazine) desorption is somewhat less competitive with ER hydrogenation, with slightly higher barriers even on Ag ($\Delta E_{\text{des}} > 0.65$ eV).

3.7. Correlations with experiments. As previously noted, the reaction energetics presented here can be used to build DFT-informed kinetic models for each metal. The complexity of the reaction networks makes it apparent that these models are necessary to fully shed light on the dominant reaction pathways as a function of reaction conditions (which affect plasma composition) and implications on relative metal performance. However, at this point we can already note that the plausible dominance of ER reactions discussed here based on DFT calculations is consistent with the lesser impact of metal composition on plasma-assisted ammonia synthesis^{20,22,26} compared to the thermocatalytic process, for which observed TOF across metals span a wide range of orders of magnitude.⁴⁹

Full understanding of the plasma-assisted ammonia synthesis mechanism (and plasma catalysts interactions) can open the door to rational manipulation of plasma conditions (reactor design) to maximize ammonia production as well as to identification of better catalysts than currently tested. The latter typically relies on the identification of a rate controlling step (RCS)⁵⁰, with catalyst modifications rationalized on the basis of boosting the RCS. Knowledge of the RCS can also facilitate computational high throughput screening using a “cheap” catalyst descriptor associated with the RCS (typically a binding energy) ref.^{51,52} However, given the breadth of reaction energetics data herein presented, we considered the empirical identification of a potential *ad hoc* descriptor that could already be used for screening.

To accomplish this, we first calculated TOFs from catalytic tests in an atmospheric pressure DBD reactor (see Section 2.1). Fe, Ni, Co, Pd, Cu and Ag were tested, with ammonia synthesis rates R_{NH_3} varying from 2.3 $\mu\text{mol}_{\text{NH}_3}/\text{min}$ in Fe to 4.5 $\mu\text{mol}_{\text{NH}_3}/\text{min}$ in Au (with energy yields varying

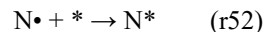
from 0.15 gNH_3/kWh to 0.30 gNH_3/kWh , respectively). A common observation to our current experiments and those earlier by us (RF)²⁰ and Iwamoto et al.²⁶ (DBD) is that an HB-inactive metal such as Ag is found to outperform an HB-active metals such as Fe.

To calculate TOFs we approximated all metal atoms as active sites, with which:

$$\text{TOF} = \frac{R_{\text{NH}_3}}{n_{\text{metal}}} \quad (7)$$

where n_{metal} is the number of moles of the metal estimated from the metal molecular weight and the mass of the metal electrodes (Fe = 4.3 g, Ni = 4.5 g, Co = 4.7 g, Pd = 5.9 g, Cu = 4.8 g, Ag = 5.3 g). This approach is consistent with our estimation of TOFs for our earlier ammonia synthesis experiments on an RF reactor, which we also examine here. Additionally, we take advantage of Iwamoto et al.²⁶ testing of a breadth of metal catalysts to convert their data to TOFs to further test descriptors. Indeed, given the variability of plasma conditions that can be tested for ammonia synthesis, we aimed to identify a descriptor that could potentially be robust to changing reaction conditions.

Earlier, Iwamoto et al.²⁶ correlated *reaction rates* with M_3N formation energy, which was calculated essentially as N^* adsorption energy on a M_3 cluster. Thus, we first tested the reaction energy for:



as a possible descriptor. The correlation (R^2) between TOFs and this descriptor was 0.59 for Iwamoto et al TOFs and 0.73 for TOFs herein but decreased to 0.38 for TOFs in our RF experiments. Given that we observed a strong correlation ($R^2 = 0.89$) between NH intensity from the OES and TOFs herein (Fig. S28), we considered also the reaction energy for:



as descriptor, but a similar scenario to that for ΔE_{rxn} of r52 occurred. At this point, we decided to test all the reaction energies at our disposal as potential descriptor and calculated their correlation factors with the above TOFs (Fig. S29). Through this exercise, we identified ΔE_{rxn} of r20 as a robust descriptor for TOFs herein ($R^2 = 0.76$), TOFs for Iwamoto et al. ($R^2 = 0.91$), and TOFs for our earlier RF experiments ($R^2 = 0.86$) as shown in Fig. 13. Note that the lower R^2 for Fig. 13a is likely due to the absence of Au, as dropping Au from Fig. 13b,c results in R^2 values similar to Fig. 13a.

Intriguingly, $r20$ is an ER hydrogenation reaction, which is a type of reaction we have shown is likely important for plasma-assisted NH_3 synthesis. But $r20$ is a hydrogenation step (HNNH_2 to HNNH_3) that is less favorable than the competing hydrogenation step $r21$ (HNNH_2 to H_2NNH_2). Without info from a kinetic model, we ascribe this to the empirical character of the descriptor. As a side note, ΔE_{rxn} of $r21$ correlates with R^2 in the 0.71 - 0.80 range for the TOFs in **Fig. 13**. In any case, it is important to note that the empiric character of the descriptor herein identified does not preclude its potential effectiveness in catalyst screening.

4. CONCLUSIONS

Detection, via optical emission spectroscopy, of plasma radicals during catalytic, plasma-assisted ammonia synthesis in a DBD reactor motivated comprehensive DFT calculations to understand the favorability of new reactions (i.e., not occurring during the traditional Haber-Bosch process) that could be facilitated by these species. These calculations were performed on nine metals, with the obtained energetics being of potential use in kinetics models that could yield a more accurate picture of the dominant pathways within the complex reaction network of this process. However, the scope of the work here was set to achieving a more granular analysis of the relative (energy-based) favorability of proposed reactions, and changes in this favorability across metals. This analysis was found to be suggestive of i) the plausibility of an associative pathway initiated by NNH formation from radical-involving reactions, ii) the likelihood of N radicals as the dominant source of N^* , iii) the probability of ER hydrogenation to be the dominant hydrogenation pathway, and iv) the likelihood of difference in dominant pathways across metals when doing plasma-assisted ammonia synthesis. Finally, the breadth of energetics data, along with catalytic experiments on six metals on a DBD reactor, allowed us to empirically identify a potentially robust (and easy to calculate) energetic descriptor (the reaction energy for HNNH_2 ER hydrogenation to HNNH_3) to discover better catalysts for these application via computational screening.

SUPPLEMENTARY INFORMATION

Electronic Supplementary Information (ESI) available: Complementary optical emission spectra. Complementary snapshots of optimized reactant, product and transition state geometries. Scaling relationships. Tabulated reaction energetics data. R^2 for correlation of TOFs with different reaction energies.

AUTHOR INFORMATION

Corresponding Author

* dgomezgualdron@mines.edu

Funding Sources

National Science Foundation, CBET.

ACKNOWLEDGMENTS

D.A.G.-G. and M.L.C. acknowledge funding from collaborative NSF grants CBET 1921484 and CBET 1947303, respectively. Simulations were made possible by the Mio supercomputer cluster at Colorado School of Mines and

NERSC computational resources from the U.S. Department of Energy (DOE). The authors thank Oscar Bender-Stone for his analysis of correlations between experimental TOF data and DFT-calculated reaction energies. Mr. Bender-Stone participated in this project through the Jefferson County Executive High School Internship Program.

REFERENCES

- (1) Sutton, M. A.; Erisman, J. W.; Dentener, F.; Möller, D. Ammonia in the environment: from ancient times to the present. *Environ. Pollut.* **2008**, *156* (3), 583–604.
- (2) Giddey, S.; Badwal, S. P. S.; Munnings, C.; Dolan, M. Ammonia as a renewable energy transportation media. *ACS Sustain. Chem. Eng.* **2017**, *5* (11), 10231–10239.
- (3) Crabtree, G. W.; Dresselhaus, M. S.; Buchanan, M. V. The Hydrogen Economy. *Phys. Today* **2004**, *57* (12), 39–44.
- (4) Ghavam, S.; Vahdati, M.; Wilson, I. A. G.; Styring, P. Sustainable ammonia production processes. *Front. Energy Res.* **2021**, *9*.
- (5) Smith, C.; Hill, A. K.; Torrente-Murciano, L. Current and future role of Haber–Bosch ammonia in a carbon-free energy landscape. *Energy Environ. Sci.* **2020**, *13* (2), 331–344.
- (6) Li, C.; Wang, T.; Gong, J. Alternative strategies toward sustainable ammonia synthesis. *Trans. Tianjin Univ.* **2020**, *26* (2), 67–91.
- (7) Carreon, M. L. Plasma catalytic ammonia synthesis: state of the art and future directions. *J. Phys. D, Appl. Phys.* **2019**, *52* (48), 483001.
- (8) Han, G.-F.; Li, F.; Chen, Z.-W.; Coppex, C.; Kim, S.-J.; Noh, H.-J.; Fu, Z.; Lu, Y.; Singh, C. V.; Siahrostami, S.; et al. Mechanochemistry for ammonia synthesis under mild conditions. *Nat. Nanotechnol.* **2021**, *16* (3), 325–330.
- (9) Zhang, Z.; Way, J. D.; Wolden, C. A. Design and operational considerations of catalytic membrane reactors for ammonia synthesis. *AIChE J.* **2021**, *67* (8).
- (10) Montoya, J. H.; Tsai, C.; Vojvodic, A.; Nørskov, J. K. The challenge of electrochemical ammonia synthesis: A new perspective on the role of nitrogen scaling relations. *ChemSusChem* **2015**, *8* (13), 2180–2186.
- (11) Murakami, K.; Tanaka, Y.; Sakai, R.; Toko, K.; Ito, K.; Ishikawa, A.; Higo, T.; Yabe, T.; Ogo, S.; Ikeda, M.; et al. The important role of N_2H formation energy for low-temperature ammonia synthesis in an electric field. *Catal. Today* **2018**.
- (12) Singh, A. R.; Rohr, B. A.; Schwalbe, J. A.; Cargnello, M.; Chan, K.; Jaramillo, T. F.; Chorkendorff, I.; Nørskov, J. K. Electrochemical ammonia synthesis—the selectivity challenge. *ACS Catal.* **2017**, *7* (1), 706–709.
- (13) Carreon, M. L. Plasma catalysis: a brief tutorial. *Plasma Res. Express* **2019**, *1* (4), 043001.

- (14) Fu, R.; Feldman, D.; Margolis, R.; Woodhouse, M.; Ardani, K. *U.S. solar photovoltaic system cost benchmark: Q1 2017*; EERE Publication and Product Library, 2017.
- (15) Zeng, Z.; Ziegler, A. D.; Searchinger, T.; Yang, L.; Chen, A.; Ju, K.; Piao, S.; Li, L. Z. X.; Ciais, P.; Chen, D.; et al. A reversal in global terrestrial stilling and its implications for wind energy production. *Nat. Clim. Chang.* **2019**, *9* (12), 979–985.
- (16) van Helden, J. H.; Wagemans, W.; Yagci, G.; Zijlmans, R. A. B.; Schram, D. C.; Engeln, R.; Lombardi, G.; Stancu, G. D.; Röpcke, J. Detailed study of the plasma-activated catalytic generation of ammonia in N₂-H₂ plasmas. *J. Appl. Phys.* **2007**, *101* (4), 043305.
- (17) Shah, J.; Wang, W.; Bogaerts, A.; Carreon, M. L. Ammonia synthesis by radio frequency plasma catalysis: revealing the underlying mechanisms. *ACS Appl. Energy Mater.* **2018**, *1* (9), 4824–4839.
- (18) Kiyooka, H.; Matsumoto, O. Reaction scheme of ammonia synthesis in the ECR plasmas. *Plasma Chem. Plasma Process.* **1996**, *16* (4), 547–562.
- (19) Tanaka, S.; Uyama, H.; Matsumoto, O. Synergistic effects of catalysts and plasmas on the synthesis of ammonia and hydrazine. *Plasma Chem. Plasma Process.* **1994**, *14* (4), 491–504.
- (20) Shah, J.; Gorky, F.; Psarras, P.; Seong, B.; Gómez-Gualdrón, D. A.; Carreon, M. L. Enhancement of the Yield of Ammonia by Hydrogen-Sink Effect during Plasma Catalysis. *ChemCatChem* **2019**.
- (21) Neyts, E. C.; Bogaerts, A. Understanding plasma catalysis through modelling and simulation—a review. *J. Phys. D, Appl. Phys.* **2014**, *47* (22), 224010.
- (22) Mehta, P.; Barboun, P.; Herrera, F. A.; Kim, J.; Rumbach, P.; Go, D. B.; Hicks, J. C.; Schneider, W. F. Overcoming ammonia synthesis scaling relations with plasma-enabled catalysis. *Nat. Catal.* **2018**, *1* (4).
- (23) van 't Veer, K.; Engelmann, Y.; Reniers, F.; Bogaerts, A. Plasma-Catalytic Ammonia Synthesis in a DBD Plasma: Role of Microdischarges and Their Afterglows. *J. Phys. Chem. C* **2020**, *124* (42), 22871–22883.
- (24) Navascués, P.; Obrero-Pérez, J. M.; Cotrino, J.; González-Elipe, A. R.; Gómez-Ramírez, A. Unraveling Discharge and Surface Mechanisms in Plasma-Assisted Ammonia Reactions. *ACS Sustain. Chem. Eng.* **2020**, *8* (39), 14855–14866.
- (25) Winter, L. R.; Ashford, B.; Hong, J.; Murphy, A. B.; Chen, J. G. Identifying surface reaction intermediates in plasma catalytic ammonia synthesis. *ACS Catal.* **2020**, *10* (24), 14763–14774.
- (26) Iwamoto, M.; Akiyama, M.; Aihara, K.; Deguchi, T. Ammonia Synthesis on Wool-Like Au, Pt, Pd, Ag, or Cu Electrode Catalysts in Nonthermal Atmospheric-Pressure Plasma of N₂ and H₂. *ACS Catal.* **2017**, *7* (10), 6924–6929.
- (27) Yamijala, S. S. R. K. C.; Nava, G.; Ali, Z. A.; Beretta, D.; Wong, B. M.; Mangolini, L. Harnessing Plasma Environments for Ammonia Catalysis: Mechanistic Insights from Experiments and Large-Scale Ab Initio Molecular Dynamics. *J. Phys. Chem. Lett.* **2020**, *11* (24), 10469–10475.
- (28) Kresse, G.; Hafner, J. *Ab initio* molecular-dynamics simulation of the liquid-metal-amorphous-semiconductor transition in germanium. *Phys. Rev. B* **1994**, *49* (20), 14251–14269.
- (29) Kresse, G.; Hafner, J. *Ab initio* molecular dynamics for liquid metals. *Phys. Rev. B* **1993**, *47* (1), 558–561.
- (30) Kresse, G.; Furthmüller, J. Efficiency of ab-initio total energy calculations for metals and semiconductors using a plane-wave basis set. *Comp. Mater. Sci.* **1996**, *6* (1), 15–50.
- (31) Perdew, J. P.; Burke, K.; Ernzerhof, M. Generalized gradient approximation made simple. *Phys. Rev. Lett.* **1996**, *77* (18), 3865–3868.
- (32) Bučko, T.; Hafner, J.; Lebègue, S.; Ángyán, J. G. Improved description of the structure of molecular and layered crystals: ab initio DFT calculations with van der Waals corrections. *J. Phys. Chem. A* **2010**, *114* (43), 11814–11824.
- (33) Grimme, S. Semiempirical GGA-type density functional constructed with a long-range dispersion correction. *J. Comput. Chem.* **2006**, *27* (15), 1787–1799.
- (34) Kerber, T.; Sierka, M.; Sauer, J. Application of semiempirical long-range dispersion corrections to periodic systems in density functional theory. *J. Comput. Chem.* **2008**, *29* (13), 2088–2097.
- (35) Methfessel, M.; Paxton, A. T. High-precision sampling for Brillouin-zone integration in metals. *Phys. Rev. B* **1989**, *40* (6), 3616–3621.
- (36) BIOVIA, Dassault Systèmes, [Materials Studio], [2017], San Diego: Dassault Systèmes, [2021].
- (37) Henkelman, G.; Uberuaga, B. P.; Jónsson, H. A climbing image nudged elastic band method for finding saddle points and minimum energy paths. *J. Chem. Phys.* **2000**, *113* (22), 9901–9904.
- (38) Henkelman, G.; Jónsson, H. A dimer method for finding saddle points on high dimensional potential surfaces using only first derivatives. *J. Chem. Phys.* **1999**, *111* (15), 7010–7022.
- (39) Wang, S.; Petzold, V.; Tripkovic, V.; Kleis, J.; Howalt, J. G.; Skúlason, E.; Fernández, E. M.; Hvolbæk, B.; Jones, G.; Toftelund, A.; et al. Universal transition state scaling relations for (de)hydrogenation over transition metals. *Phys. Chem. Chem. Phys.* **2011**, *13* (46), 20760–20765.
- (40) Medford, A. J.; Vojvodic, A.; Hummelshøj, J. S.; Voss, J.; Abild-Pedersen, F.; Studt, F.; Bligaard, T.; Nilsson, A.; Nørskov, J. K. From the Sabatier principle to a predictive theory of transition-metal heterogeneous catalysis. *J. Catal.* **2015**, *328*, 36–42.

- (41) Garden, A. L.; Skúlason, E. The mechanism of industrial ammonia synthesis revisited: calculations of the role of the associative mechanism. *J. Phys. Chem. C* **2015**, *119* (47), 26554–26559.
- (42) Back, S.; Jung, Y. On the mechanism of electrochemical ammonia synthesis on the Ru catalyst. *Phys. Chem. Chem. Phys.* **2016**, *18* (13), 9161–9166.
- (43) Psarras, P.; Anderson, R.; Gómez-Gualdrón, D. A.; Wilcox, J. Material Consequences of Hydrogen Dissolution in Palladium Alloys Observed from First Principles. *J. Phys. Chem. C* **2019**, *123* (36), 22158–22171.
- (44) Yeo, S. C.; Han, S. S.; Lee, H. M. Adsorption, dissociation, penetration, and diffusion of N₂ on and in bcc Fe: first-principles calculations. *Phys. Chem. Chem. Phys.* **2013**, *15* (14), 5186–5192.
- (45) Jiang, D. E.; Carter, E. A. Diffusion of interstitial hydrogen into and through bcc Fe from first principles. *Phys. Rev. B* **2004**, *70* (6), 064102.
- (46) Molecular theory of gases and liquids. J. O. Hirschfelder, C. F. Curtiss, and R. B. Bird. Wiley, New York, 1954. xxvi + 1219 pp., \$20.00. *J. Polym. Sci.* **1955**, *17* (83), 116–116.
- (47) Loenders, B.; Engelmann, Y.; Bogaerts, A. Plasma-Catalytic Partial Oxidation of Methane on Pt(111): A Microkinetic Study on the Role of Different Plasma Species. *J. Phys. Chem. C* **2021**, *125* (5), 2966–2983.
- (48) Uyama, H.; Nakamura, T.; Tanaka, S.; Matsumoto, O. Catalytic effect of iron wires on the syntheses of ammonia and hydrazine in a radio-frequency discharge. *Plasma Chem. Plasma Process.* **1993**, *13* (1), 117–131.
- (49) Dahl, S.; Logadottir, A.; Jacobsen, C. J. H.; Nørskov, J. K. Electronic factors in catalysis: the volcano curve and the effect of promotion in catalytic ammonia synthesis. *Applied Catalysis A: General* **2001**, *222* (1–2), 19–29.
- (50) Campbell, C. T. The degree of rate control: A powerful tool for catalysis research. *ACS Catal.* **2017**, *7* (4), 2770–2779.
- (51) ANDERSSON, M.; BLIGAARD, T.; KUSTOV, A.; LARSEN, K.; GREELEY, J.; JOHANNESSEN, T.; CHRISTENSEN, C.; NORSKOV, J. Toward computational screening in heterogeneous catalysis: Pareto-optimal methanation catalysts. *J. Catal.* **2006**, *239* (2), 501–506.
- (52) Chen, B. W. J.; Xu, L.; Mavrikakis, M. Computational methods in heterogeneous catalysis. *Chem. Rev.* **2021**, *121* (2), 1007–1048.